International Journal of Nanomedicine

Dovepress

open access to scientific and medical research

Open Access Full Text Article

ORIGINAL RESEARCH

# Surface-Modified Nano-Hydroxyapatite Uniformly Dispersed on High-Porous GelMA Scaffold Surfaces for Enhanced Osteochondral Regeneration

Suyang Zheng[1,*], Dong Li[1,2,*], Qingbai Liu[1,3], Cheng Tang[1], Wenhao Hu[1,4], Shengshan Ma[1,5], Yan Xu[1,6,7], Yong Ma[8], Yang Guo[8], Bo Wei[1], Chuanlin Du[9], Liming Wang[1,6,7]

[1]Department of Orthopedics, Nanjing First Hospital, Nanjing Medical University, Nanjing, Jiangsu Province, People's Republic of China; [2]Department of Trauma Center, The Affiliated Changzhou No.2 People's Hospital of Nanjing Medical University, Changzhou, Jiangsu Province, People's Republic of China; [3]Department of Orthopedics, Lianshui People's Hospital of Kangda College Affiliated to Nanjing Medical University, Huai'an, Jiangsu Province, People's Republic of China; [4]Department of Orthopedics, The Affiliated Huai'an No.1 People's Hospital of Nanjing Medical University, Huai'an, Jiangsu Province, People's Republic of China; [5]Department of Sports Medicine, The First People's Hospital of Lianyungang, The Affiliated Lianyungang Hospital of Xuzhou Medical University, Lianyungang, Jiangsu Province, People's Republic of China; [6]Key Laboratory of Additive Manufacturing Technology, Institute of Digital Medicine, Nanjing Medical University, Nanjing, Jiangsu Province, People's Republic of China; [7]Cartilage Regeneration Center, Nanjing First Hospital, Nanjing Medical University, Nanjing, Jiangsu Province, People's Republic of China; [8]Laboratory of New Techniques of Restoration and Reconstruction of Orthopedics and Traumatology, Nanjing University of Chinese Medicine, Nanjing, Jiangsu Province, People's Republic of China; [9]Department of Orthopedics, Ganyu District People's Hospital of Lianyungang, Lianyungang, Jiangsu Province, People's Republic of China

*These authors contributed equally to this work

Correspondence: Liming Wang; Chuanlin Du, Tel +86-25-5227-1000; +86-518-8621-2626, Fax +86-25-5226-9924; +86-518-8622-5984, Email wlmnjsy@outlook.com; chuanlindu@foxmail.com



**Purpose:** This study aims to investigate the impact of enhancing subchondral bone repair on the efficacy of articular cartilage restoration, thereby achieving improved osteochondral regeneration outcomes.

**Methods:** In this study, we modified the surface of nano-hydroxyapatite (n-HAp) through alkylation reactions to prepare n-HApMA. Characterization techniques, including X-ray diffraction, infrared spectroscopy scanning, thermogravimetric analysis, particle size analysis, and electron microscopy, were employed to analyze n-HApMA. Bioinks were prepared using n-HApMA, high porosity GelMA hydrogel, and adipose tissue derived stromal cells (ADSCs). The rheological properties of the bioinks during photocuring were investigated using a rheometer. Based on these bioinks, a biphasic scaffold was constructed. The viability of cells within the scaffold was observed using live-dead cell staining, while the internal morphology was examined using scanning electron microscopy. The stiffness of the scaffold was evaluated through compression testing. Scaffolds were implanted into the osteochondral defects of New Zealand rabbit knees, and microCT was utilized to observe the subchondral bone repair. Hematoxylin and eosin (H&E) staining, Masson's trichrome staining, and Safranin O/Fast Green staining were performed to assess the regeneration of subchondral bone and cartilage. Furthermore, immunohistochemical staining was employed to detect the expression of osteogenic and chondrogenic-related molecules.

**Results:** Scaffold characterization revealed that surface modification enables the uniform distribution of n-HApMA within the GelMA matrix. The incorporation of 5% n-HApMA notably enhanced the elastic modulus and stiffness of the 6% high-porosity GelMA in comparison to n-HAp. Moreover, in-vivo study showed that the homogeneous dispersion of n-HApMA on the GelMA matrix facilitated the osteogenic differentiation of adipose-derived stem cells (ADSCs) and promoted osteochondral tissue regeneration.

**Conclusion:** These findings suggest potential applications of the n-HApMA/GelMA composite in the field of tissue engineering and regenerative medicine.

**Keywords:** subchondral bone, surface modification, bio-ink, scaffold, hydrogel

## Introduction

Osteoarthritis (OA) is a prevalent age-related degenerative disease causing joint pain and cartilage breakdown, leading to a substantial economic impact.[1] Current clinical treatment follows a stepwise approach based on disease stage and

Received: 6 July 2023
Accepted: 7 October 2023
Published: 21 October 2023

**Graphical Abstract**

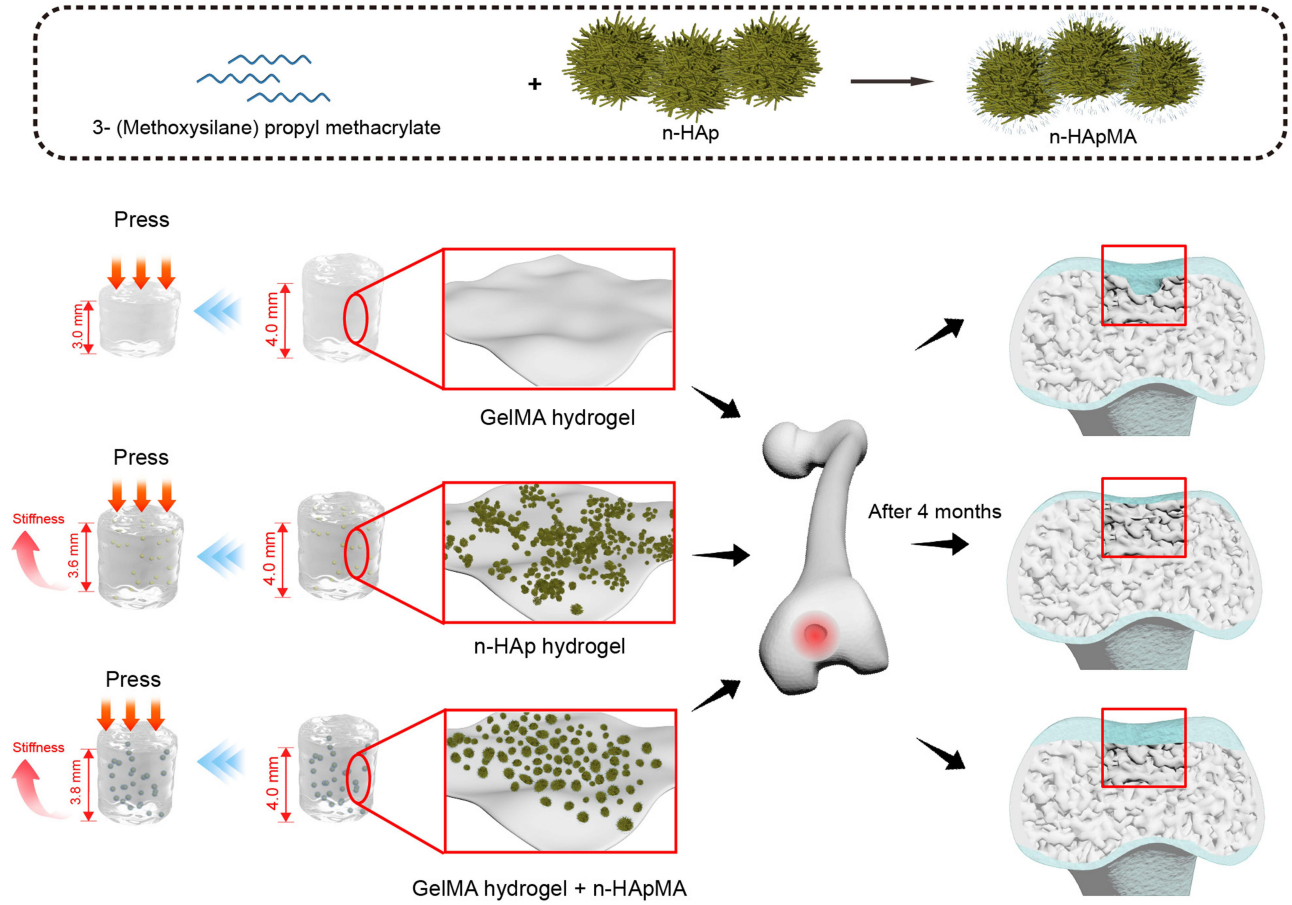


severity, aiming to improve outcomes, alleviate symptoms, and enhance patients' quality of life.[2] In cases of severe cartilage damage and bone marrow edema, patients may require reconstructive therapies, such as joint replacement surgery, which effectively alleviates pain but entails inherent risks.[3] Regenerative therapy, involving tissue engineering technology, aims to repair damaged cartilage and subchondral bone by employing a combination of scaffolds, seed cells, and growth factors, offering more effective treatment options and reducing surgical risks.[4,5]

Tissue engineering scaffolds offer a structural basis for new tissue development, composed of biomaterials like collagen, gelatin, and polylactic acid. Ideal scaffolds should exhibit biodegradability and high permeability.[6] Appropriate seed cells include chondrocytes and mesenchymal stem cells (MSCs). MSCs are preferred due to their superior proliferative abilities.[7] Tissue engineering scaffolds often incorporate growth factors, such as transforming growth factor-beta (TGF-β), insulin-like growth factor-1 (IGF-1), and bone morphogenetic proteins (BMPs), to assist with seed cell proliferation and differentiation.[6]

In recent years, there has been growing recognition of the importance of subchondral bone in cartilage repair. However, the precise role of subchondral bone in the development and progression of OA remains unclear. The interaction between bone and cartilage is critical, and the subchondral bone microenvironment plays a central role in this process, as suggested by several studies.[8–14] Moreover, research has revealed a mutual regulatory relationship between cartilage and subchondral bone.[15]

It is crucial to identify methods that promote subchondral bone repair in order to further demonstrate its role in cartilage repair. Hydroxyapatite (HAp) displays favorable biological properties, such as osteoconduction, osteointegration, and

osteoinduction, without any reported toxicity.[16–19] Nanoscale hydroxyapatite (n-HAp) has been shown to significantly promote osteocyte formation.[20] However, its high surface energy makes it prone to aggregation in aqueous solutions, which may potentially have an impact on cell proliferation and differentiation when used with certain concentrations of dispersants.[21] Previous research indicates that when the surface of modified HAp samples becomes more structurally and chemically similar to the polymer component of the polymer network in which it is used as a filler, the cross-linking process resembles more closely the cross-linking of an unfilled polymer.[22] To achieve a more uniform dispersion of n-HAp within the GelMA surface, it is advantageous to introduce methacrylate groups onto the n-HAp surface, which are the same type of groups involved in cross-linking with GelMA. Past literature has validated the reproducibility of silane coupling agents for n-HAp surface modification,[23] as well as their anti-aggregation properties.[24] Therefore, the silane coupling agent, 3-(Trimethoxysilyl)propyl methacrylate, possessing methacrylate groups, becomes an ideal choice for this application.

Scaffold porosity and interconnectivity are also essential factors influencing bone growth and angiogenesis.[25,26] Angiogenesis requires a minimum pore size of approximately 50 microns, while osteoid growth necessitates around 200 microns.[27] Pore size also affects bioactivity, protein interaction, cell attraction, directional and oriented cell and bone ingrowth, mechanical strengthening, and implant shape and aesthetics.[28]

Drawing on the mechanisms discussed above regarding the role of subchondral bone in cartilage repair, we performed surface chemical modification of nanoscale hydroxyapatite to enhance its dispersibility in hydrogels. Subsequently, we employed tissue engineering methodologies to fabricate a biphasic osteochondral integrated regeneration scaffold. This scaffold establishes an optimal subchondral bone microenvironment, supporting both subchondral bone and cartilage regeneration.

# Materials and Methods

## Synthesis of Methacrylated Nano-Hydroxyapatite (n-HApMA)

Twelve grams of nanoscale hydroxyapatite (H106378, Aladdin, Shanghai, China) was dispersed in 100mL of water by ultrasonication for 10 minutes. Then, 12g of sodium citrate was dissolved in 140mL of water and rapidly added to the dispersed hydroxyapatite, while ultrasonication was continued for 30 minutes, followed by mechanical stirring for 2 hours. The resulting powder was washed four times with distilled water by centrifugation and then dried overnight at 80°C. The powder was then dispersed in water to form a 50g/L suspension, which was subjected to ultrasonication for 10 minutes. The suspension was adjusted to pH 4 using a 5% acetic acid buffer solution and then subjected to ultrasonication for an additional 30 minutes. One milliliter of 3-(Trimethoxysilyl)propyl methacrylate (S111153, Aladdin, Shanghai, China) was added, and the reaction mixture was kept at a constant temperature of 80°C under stirring conditions of 450 rpm for 4 hours. The resulting mixture was then subjected to ultrafiltration and washing, and the solid product was extracted with ethanol and dried at 80°C.

## Characterization of n-HApMA

### Particle Size, PDI, and Zeta Potential

The particle size distribution, PDI, and zeta potential of the unmodified and modified nanoscale hydroxyapatite were determined using a Brookhaven Instruments Zeta Plus dynamic light scattering (DLS) instrument (Brookhaven, New York, USA) after sonication in pure water.

### Transmission Electron Microscopy (TEM)

The morphology of the unmodified and modified nanoscale hydroxyapatite powders was observed using a transmission electron microscope (JEM-2100, JEOL, Tokyo, Japan) after sonication for 30 minutes and drop casting of 1–2 drops of the suspension onto a copper grid for natural drying.

### Scanning Electron Microscopy (SEM)

The surface morphology of the unmodified and modified nanoscale hydroxyapatite was observed using a scanning electron microscope (JSM-7500F, JEOL, Tokyo, Japan) after sample preparation.

### X-Ray Diffraction (XRD)

The phase structures of the unmodified and modified nanoscale hydroxyapatite were determined using an X-ray diffraction spectrometer (XRD-7000, Shimadzu, Kyoto, Japan) with a scanning rate of 2 (°)/min and a scanning range of 10°–90°.

### Fourier-Transform Infrared Spectroscopy (FTIR)

The FTIR spectra of the unmodified and modified nanoscale hydroxyapatite were obtained using the FTIR spectrometer (Spectrum Two, PerkinElmer, Waltham, MA, USA) with a scanning range of 400–4000 $cm^{-1}$.

### Thermogravimetric Analysis (TGA)

Thermogravimetric analysis was performed using a Mettler Toledo TGA/DSC3+ instrument (Zurich, Switzerland) under a nitrogen atmosphere from room temperature to 800 °C with a heating rate of 10 °C/min to obtain the thermogravimetric (TG) and differential scanning calorimetry (DSC) curves.

### Weight Gain

The mass of the unmodified and modified nanoscale hydroxyapatite was measured using an electronic analytical balance (CP114, OHAUS, Parsippany, NJ, USA). The weight gain was calculated as (m1 − m0)/m0 × 100%, where m0 is the mass of the unmodified powder and m1 is the mass of the modified powder.

## Isolation and Culture of Primary ADSCs

The synovial connective tissue is removed from the inguinal adipose pad of adult New Zealand rabbits, and the remaining adipose tissue is placed in a 50 mL centrifuge tube. Sterile PBS is added, and the sample is centrifuged at 1000 rpm for 5 minutes. The floating fat layer on the top is transferred to another 50 mL centrifuge tube and centrifuged again. This process is repeated 3 times to remove red blood cells from the adipose tissue. The adipose tissue is then minced and centrifuged once more with the addition of PBS. The top fat layer is poured into a T75 culture flask, and a digestion solution containing 0.1% type I collagenase and 0.25% trypsin is added, submerging the adipose tissue completely. The culture flask is placed vertically in a 37°C incubator with shaking for 1 hour. Afterward, 10% fetal bovine serum (FBS) is added to stop the digestion, and the digestion solution is transferred to a 50 mL centrifuge tube and centrifuged at 1800 rpm for 10 minutes. The upper fat layer and supernatant are discarded, and 20 mL PBS is added to the tube for resuspension, followed by centrifugation at 1000 rpm for 10 minutes. Finally, the supernatant is discarded, and the cells are resuspended in low-glucose DMEM complete medium with 10% FBS. The cells are seeded in a 6-well plate at a density of $5 \times 10^5$ cells per well and incubated at 37°C and 5% CO2. The culture medium is changed every two days, and subculturing is performed when the cells reach over 70% confluence.

## Preparation and Characterization of Bio-Inks

A high-porosity GelMA hydrogel (GMPR-002, EFL, Suzhou, China) is prepared by dissolving 0.6 g of GelMA and 25 mg of LAP in 10 mL of PBS, followed by magnetic stirring at 37°C for 1 hour in a water bath. The solution is then filtered for sterilization. To prepare the bio-ink PR-GelMA6, $1 \times 10^7$ ADSCs are resuspended in 10 mL of GelMA hydrogel. For the preparation of bio-ink n-HAp5, 5% (w/v) of n-HAp is added to the GelMA hydrogel, and the mixture is homogenized. Then, $1 \times 10^6$/mL ADSCs are resuspended in the hydrogel. To prepare bio-ink n-HApMA5, 5% (w/w) n-HApMA is added to the GelMA hydrogel and mixed evenly. Subsequently, $10^6$/mL ADSCs are resuspended in the hydrogel. The compositions of the three bio-inks are summarized in Table 1.

A 150 μL sample of each bio-ink is used for rheological testing at a constant temperature of 25°C. During the 0–30-second interval, no light is applied; from 30 to 60 seconds, 405 nm light at 25 $mW/cm^2$ is applied; and from 60 to 75 seconds, light exposure is stopped.

## Scaffold Construction

Open-ended cylindrical containers with an inner diameter of 4 mm, a height of 4 mm, and a wall thickness of 0.3 mm are fabricated by a 3D printer (BP6601, EFL, Suzhou, China) using PCL and sterilized with gamma irradiation. These

**Table 1** Formula of Bio-Inks

| Bio-Inks | DMEM | GelMA | LAP | ADSCs | n-HAp | n-HApMA |
|---|---|---|---|---|---|---|
| PR-GelMA6 | 10mL | 600mg | 25mg | $1 \times 10^7$ | - | - |
| n-HAp5 | 10mL | 600mg | 25mg | $1 \times 10^7$ | 500mg | - |
| n-HApMA5 | 10mL | 600mg | 25mg | $1 \times 10^7$ | - | 500mg |

**Abbreviations**: DMEM, Dulbecco's Modified Eagle Medium; GelMA, methacrylated gelatin; LAP, lithium phenyl-2,4,6-trimethylbenzoylphosphinate; ADSCs, adipose-derived stem cells; n-HAp, nano-hydroxyapatite; n-HApMA, methacrylated nano-hydroxyapatite.

containers are then placed on a sterile glass plate. A 10 μL pipette is used to add the prepared bio-ink into the containers. For every 10 μL of bio-ink added, a 25 mW/cm$^2$ 405nm light source is applied 5 cm above the container for 20 seconds to cure the bio-ink. This process is repeated until the container is filled with bio-ink.

## Scaffold Characterization

### Live/Dead Staining

Carefully remove the scaffolds from the containers and place them in a 24-well plate, submerged in 1 mL of DMEM culture medium. Incubate the 24-well plate in a 37°C, 5% $CO_2$ incubator with daily medium changes. After three days of cultivation, stain the scaffolds using a live-dead staining kit. Then, observe and capture images under a confocal microscope (FV1000, Olympus, Tokyo, Japan).

### Scanning Electron Microscopy (SEM)

Cut the prepared scaffolds horizontally, freeze-dry them, and take cross-sectional images using scanning electron microscopy (SU8100, Gatan, Pleasanton, CA, USA).

### Compression Testing

Place the constructed scaffolds on a universal material testing machine (Jitai-5kn, Jimtec, China). Using a 3 mm diameter stainless steel rod, apply a 5 mm/min compression to the scaffolds and record the displacement-load data.

## In vivo Experiments

### Ethical Considerations

The experimental procedures involving the use of New Zealand rabbits in this study were approved by the Ethics Committee of Nanjing First Hospital. All necessary measures were taken to ensure the well-being and humane treatment of the animals throughout the study. The guidelines provided in the NIH Guide for the Care and Use of Laboratory Animals were followed to minimize any potential distress or harm to the animals involved in the research.

### Surgical Procedures

Eighteen New Zealand rabbits (2.5–3kg, six months) were randomly divided into 3 groups, with 6 in each group. After the anesthetic procedure, a midline incision is made on the knee to expose the joint cavity, and a 4 mm diameter, 4-mm-deep hole is drilled in the intercondylar region of the distal femur to create a bone and cartilage defect in the rabbit. Scaffolds constructed with PR-GelMA6 bio-ink are placed in the control group, n-HAp5 bio-ink scaffolds in the n-HAp group, and n-HApMA5 bio-ink scaffolds in the n-HApMA group. After washing with saline solution, the layers are sutured, and erythromycin ointment is applied to the incision. Daily intramuscular injections of penicillin are administered for three days. At 2 and 4 months post-surgery, the experimental animals are euthanized, the distal femur is isolated, photographed, and fixed in 4% paraformaldehyde.

### MicroCT

Distal femur specimens are scanned using microCT (SkyScan 1176, Bruker, Belgium), and cross-sectional images of the defect site are obtained. A separate 3D reconstruction of the defect site is performed, and the parameters of trabecular thickness (Tb.Th) and bone volume to total volume (BV/TV) are calculated for the area.

### Histopathological Evaluation

The samples, once fixed, undergo a three-month decalcification process using 10% EDTA solution. Subsequent steps include dehydration, clearing, paraffin infiltration, sectioning, and slide mounting. The mounted sections are deparaffinized, rehydrated, and sequentially stained with hematoxylin and eosin, Masson's trichrome, and Safranin O/Fast Green. The sections are then once again dehydrated, cleared, and mounted under a coverslip for microscopic examination. Immunohistochemical staining is used to visualize Runx2, Sox9, OCN, Aggrecan, Col1, and Col2 proteins. Images of the specimens were captured using a fully automated digital histology slide scanner (VS200, Olympus, Japan). All tissue sections are consistently cut through the cylindrical defect that was formed during the modeling process. Each section plane aligns parallel to the longitudinal axis of this defect and concurrently with the coronal axis of the femoral condyle. Sequential and mutually parallel tissue sections are utilized for the aforementioned variety of stains, ensuring that different staining types can reveal the structure of the identical location, thus providing a comprehensive representation of the area under examination.

## Statistical Analysis

Statistical analysis was performed using Prism 9.0. Differences between groups were analyzed by one-way ANOVA. The normality test (Shapiro–Wilk) was used for one-way ANOVA. Statistical significance was set at $p < 0.05$.

# Results

## Characterization of n-HApMA

The surface of nano-hydroxyapatite (n-HAp) was successfully chemically modified using an alkyl coupling method. The zeta potential of unmodified n-HAp was −8.54 mV, while that of the modified n-HApMA was −11.73 mV (Figure 1f). The chemical modification reduced the average particle size of n-HAp from 1131 nm to 813.1 nm for n-HApMA (Figure 1e). The PDI changed from 0.3149 to 0.5422. The DLS results showed that the modified n-HApMA had a smaller particle size and better dispersion compared to unmodified n-HAp.

SEM and TEM images revealed no significant changes in particle size for n-HAp before and after modification, consistent with the average particle size values obtained from DLS results (Figure 1a–d).

FTIR results demonstrated that the broad peak at 3435 $cm^{-1}$ for unmodified n-HAp represented the stretching vibration peak of –OH, while the peaks at 1035 $cm^{-1}$ and 1091 $cm^{-1}$ were attributed to the asymmetric stretching vibration absorption peaks of $PO_4^{3-}$, and the peaks at 612 $cm^{-1}$ and 567 $cm^{-1}$ corresponded to the bending vibration absorption peaks of the P-O bond in $PO_4^{3-}$. The characteristic peaks of n-HAp were observed at 1642 $cm^{-1}$, 1091 $cm^{-1}$, 1044 $cm^{-1}$, 1035 $cm^{-1}$, 612 $cm^{-1}$, and 567 $cm^{-1}$. No significant changes in absorption peaks were observed for n-HApMA after modification, and the absorption peaks mainly reflected the characteristics of hydroxyapatite (Figure 1g).

XRD results showed that the characteristic peaks of HAP appeared at 2θ values of 25.9°, 31.8°, 34.1°, 46.7°, and 49.5° for n-HAp. A comparison before and after modification revealed no changes in the diffraction peak positions, indicating that the chemical modification did not alter the crystal structure or crystallinity of n-HAp (Figure 1h).

The thermogravimetric curve of the n-HAp sample showed that the weight loss was 4.85% below 800°C, with faster weight loss below 350°C, which may be related to the HA crystal structure. The weight loss of the n-HApMA sample was 4.64%, with a linear weight loss below 300°C, mainly due to the water inside of n-HApMA. Rapid decomposition occurred between 360°C and 600°C, with thermal decomposition mainly caused by the decomposition of the surface coupling agent molecules (Figure 1i). DSC results showed that the weight loss rates of n-HAp and n-HApMA were very similar. The differential thermal curves before and after modification revealed exothermic peaks at 300°C and 500°C, which were close to the peak maximum weight loss rates in the TG curve. The differences between the two samples indicated a possible relationship with surface modification (Figure 1j).

The mass of n-HAp before chemical modification was 10 g, and after modification, the mass of n-HApMA was 10.08 g, resulting in a weight increase of 0.8%.

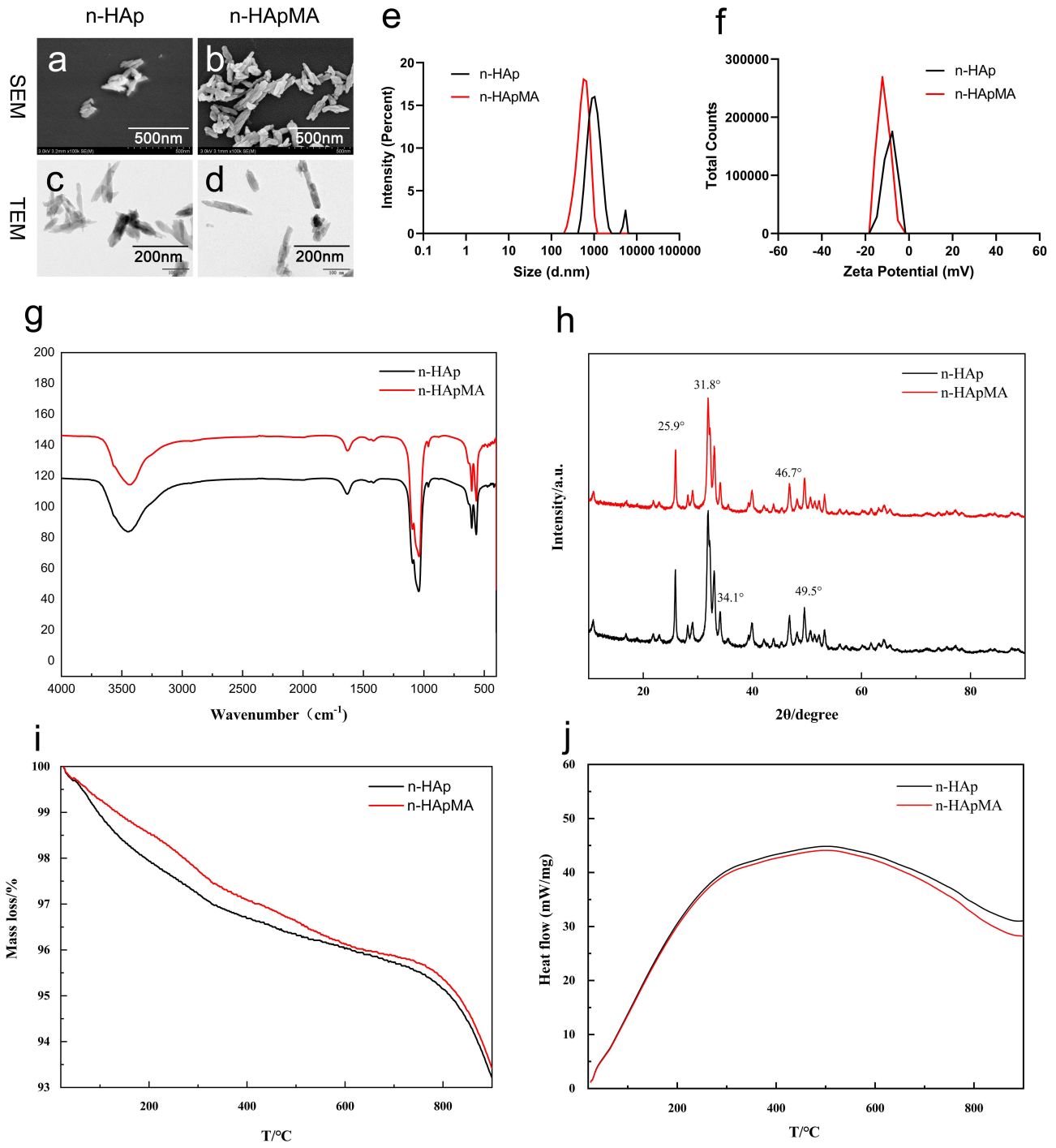


**Figure 1** Characterization of nano-hydroxyapatite (n-HAp) and methacrylated nano-hydroxyapatite (n-HApMA). (**a–d**) Scanning electron microscope (SEM) and transmission electron microscope (TEM) images, (**e**) particle size distribution, (**f**) zeta potential, (**g**) infrared spectra, (**h**) X-ray diffraction patterns, (**i**) thermogravimetric analysis, (**j**) differential scanning calorimetry curves.

## Characterization of the Bio-Inks

The rheological curves showed that the time of phase transition for the high-porosity GelMA did not change significantly after the addition of n-HAp and n-HApMA. However, the final elasticity and viscosity of the samples increased significantly after photocuring. Among them, the storage modulus of high-porosity GelMA containing 5% n-HApMA

reached approximately three times that of the control group after complete curing, while the high-porosity GelMA containing 5% n-HAp was about twice that of the control group (Figure 2a and b).

Compression test results were consistent with the rheological results. Scaffolds constructed with n-HApMA5 bio-ink exhibited the highest slope of the displacement–load curve during compression, followed by n-HAp5, and the control group had the lowest slope. This suggests that the addition of 5% n-HApMA led to a significant increase in the stiffness of the high-porosity GelMA hydrogel, while the improvement in stiffness achieved by adding 5% n-HAp was not as pronounced as that with 5% n-HApMA (Figure 2c and d).

## Scaffold Characterization

After the addition of n-HAp and n-HApMA, the transparency of the high-porosity GelMA hydrogels decreased, and a gradient feature was observed at the interface (Figure 3a–c).

Confocal microscopy was employed to simultaneously visualize live adipose-derived stem cells (ADSCs) stained green in the cytoplasm, and dead cells stained red in the nucleus. Cell viability was quantified as the percentage of green cells relative to the total cell population. The cells in the bio-inks containing n-HAp and n-HApMA maintained a relatively good morphology (Figure 3d–f). A one-way ANOVA was conducted to compare the viability across three groups, revealing no statistically significant differences ($P > 0.05$). This suggests that the inclusion of n-HAp and n-HApMA into the bio-inks did not adversely impact the viability of ADSCs, thus demonstrating their safety for use in cell culture applications.

Scanning electron microscopy images revealed that all three scaffolds exhibited excellent porosity. The pore size of the hydrogels did not change significantly after the addition of n-HAp and n-HApMA (Figure 3g–i). However, there were noticeable differences in the microstructures of the three scaffolds. The control group hydrogel surface appeared

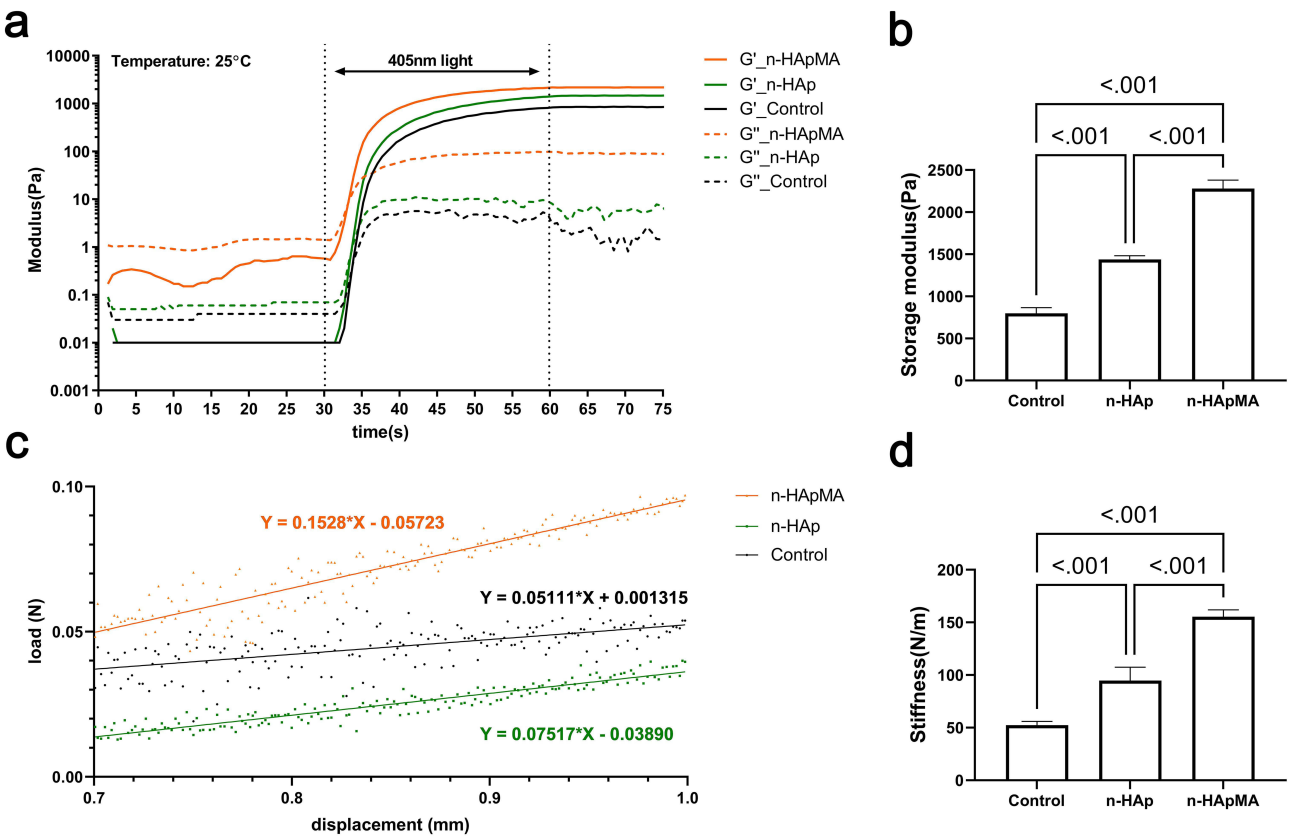


**Figure 2** Properties of high-porosity GelMA mixed with nano-hydroxyapatite (n-HAp) and methacrylated nano-hydroxyapatite (n-HApMA). (**a**) Photocuring rheological curve at 25°C, (**b**) storage modulus, (**c**) displacement–load curve, (**d**) stiffness.

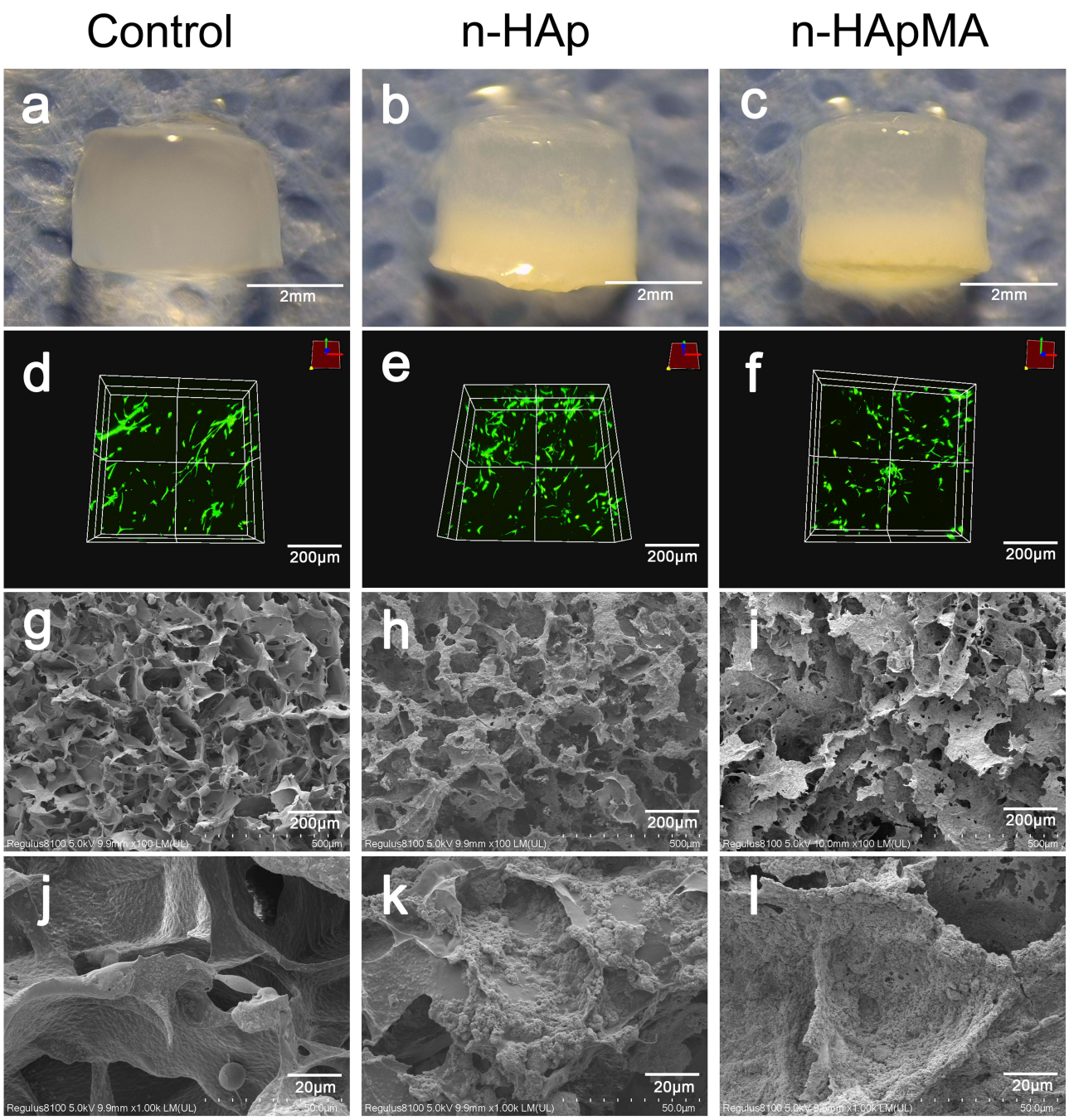


**Figure 3** Scaffold and cell visualization in control, nano-hydroxyapatite (n-HAp), and methacrylated nano-hydroxyapatite (n-HApMA) groups. (**a–c**) Gross scaffold appearance, (**d–f**) three-dimensional reconstruction of adipose-derived stem cells (ADSCs) live/dead staining, (**g–l**) scanning electron microscope (SEM) images of scaffold.

smoother, while the addition of 5% n-HAp resulted in an uneven coverage of n-HAp particles on the hydrogel surface, with visible aggregation and some areas where the hydrogel did not cover the n-HAp particles. After adding 5% n-HApMA, the hydrogel surface uniformly covered the n-HApMA particles, and no obvious aggregation was observed (Figure 3j–l).

## Gross Photographs and CT in Animal Experiments

At two months post-surgery, there was no observable cartilage repair in the control and n-HAp groups, while the n-HApMA group displayed a relatively complete cartilage coverage (Figure 4a–c). Four months post-surgery,

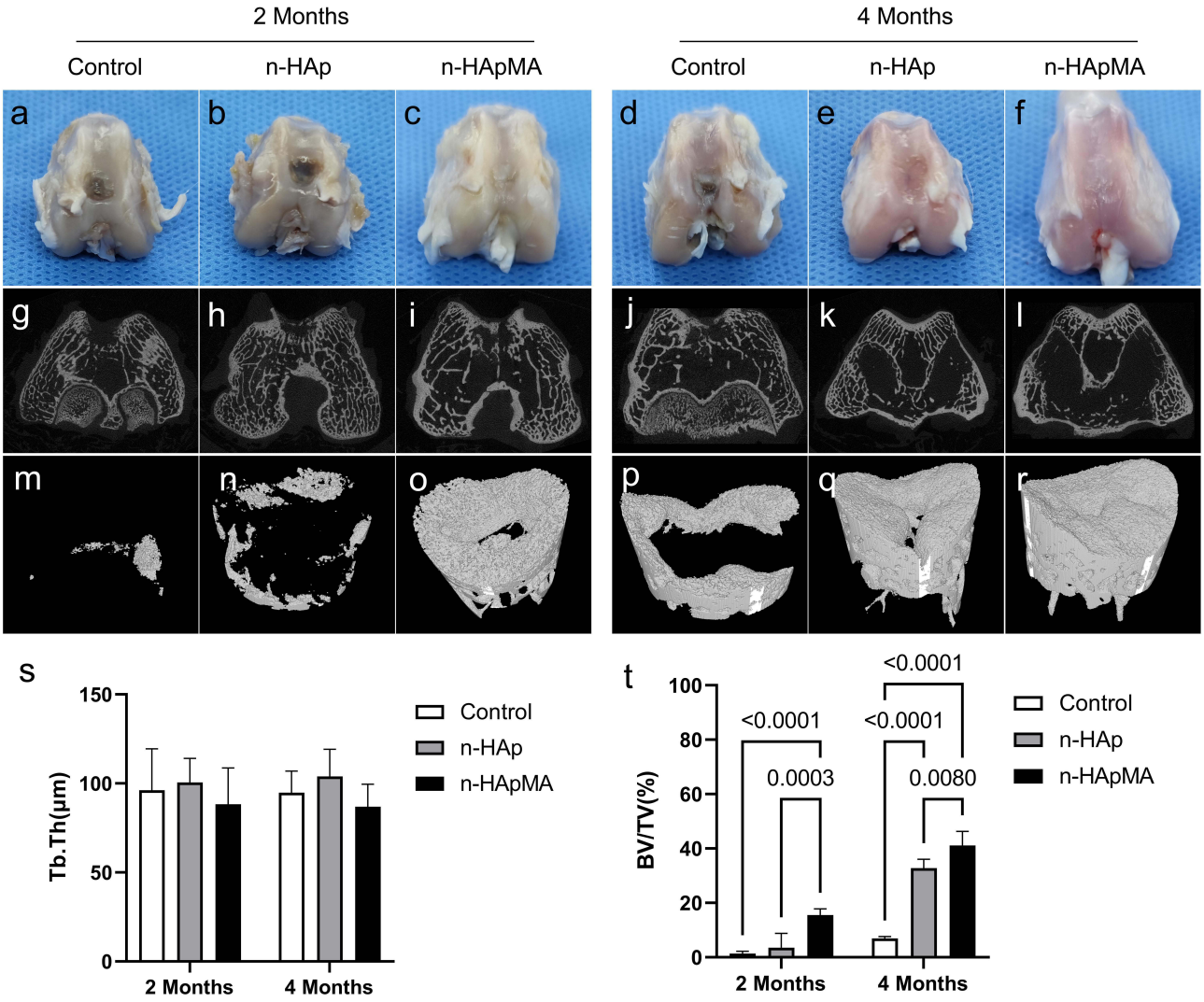


**Figure 4** Evaluation of femoral condyle samples at 2 and 4 months post-treatment. (**a–f**) Gross appearance, (**g–l**) micro-CT cross-sectional views, (**m–r**) three-dimensional reconstruction of bone-cartilage defect modeling regions using micro-CT, (**s**) trabecular thickness (Tb.Th), (**t**) bone volume/total volume (BV/TV) in regenerated regions.

the cartilage surface in the control group exhibited some repair but was not complete, while the cartilage surfaces in the n-HAp and n-HApMA groups were fully repaired, with the n-HApMA group appearing closer to the uninjured state (Figure 4d–f).

MicroCT results showed that, at two months post-surgery, the control group had almost no bone regeneration, the n-HAp group displayed a small amount of bone regeneration, and the n-HApMA group demonstrated significantly better bone regeneration than the control and n-HAp groups (Figure 4g–i and 4m–o). At four months post-surgery, the control group showed a small amount of bone regeneration, the n-HAp group had a significant amount of bone regeneration compared to the control group, and the n-HApMA group exhibited the best bone regeneration, close to complete regeneration, with significantly better results than the n-HAp and control groups (Figure 4j–l and 4p–r).

Quantitative analysis of the regenerated bone tissue in the defect area was performed using the BoneJ plugin in ImageJ. The results showed no significant change in trabecular thickness (Tb.Th) among the groups, but there were significant differences in bone volume/total volume (BV/TV). At two months post-surgery, the n-HApMA group was significantly higher than the n-HAp and control groups. At four months post-surgery, the n-HApMA group was significantly higher than the n-HAp and control groups, while the n-HAp group was significantly higher than the control group (Figure 4s and t).

## Histological Staining

Adjacent sections from the same sample underwent hematoxylin and eosin (H&E) staining, Safranin O/Fast Green staining, Masson's trichrome staining, and immunohistochemical staining for display. The planes of these sections were carefully matched to the slice locations presented in the CT results. Each sample from every group was represented by two images: a comprehensive view that covers the entire osteochondral defect modeling area and a selected view from the same comprehensive image, aimed at showing the differences between the modeled and non-modeled areas and the healing status of the cartilage layer and subchondral bone.

HE staining results showed that at two months post-surgery, cells in the control group's regenerated area were arranged chaotically, with cartilage-like lacunae structures appearing in the deep layer, and cells densely packed in the superficial layer, similar to normal cartilage tissue. The n-HAp group's cartilage regeneration area displayed uneven cell distribution, with lower similarity to cartilage. In the n-HApMA group's regenerated area, cells were uniformly distributed with numerous cartilage-like lacunae structures in the deep layer, but the superficial layer cells were not more densely packed than the deep layer (Figure 5a–c). At four months post-surgery, cell density in the control group's cartilage regeneration area decreased, with superficial cells becoming sparse. The n-HAp group's regenerated cartilage

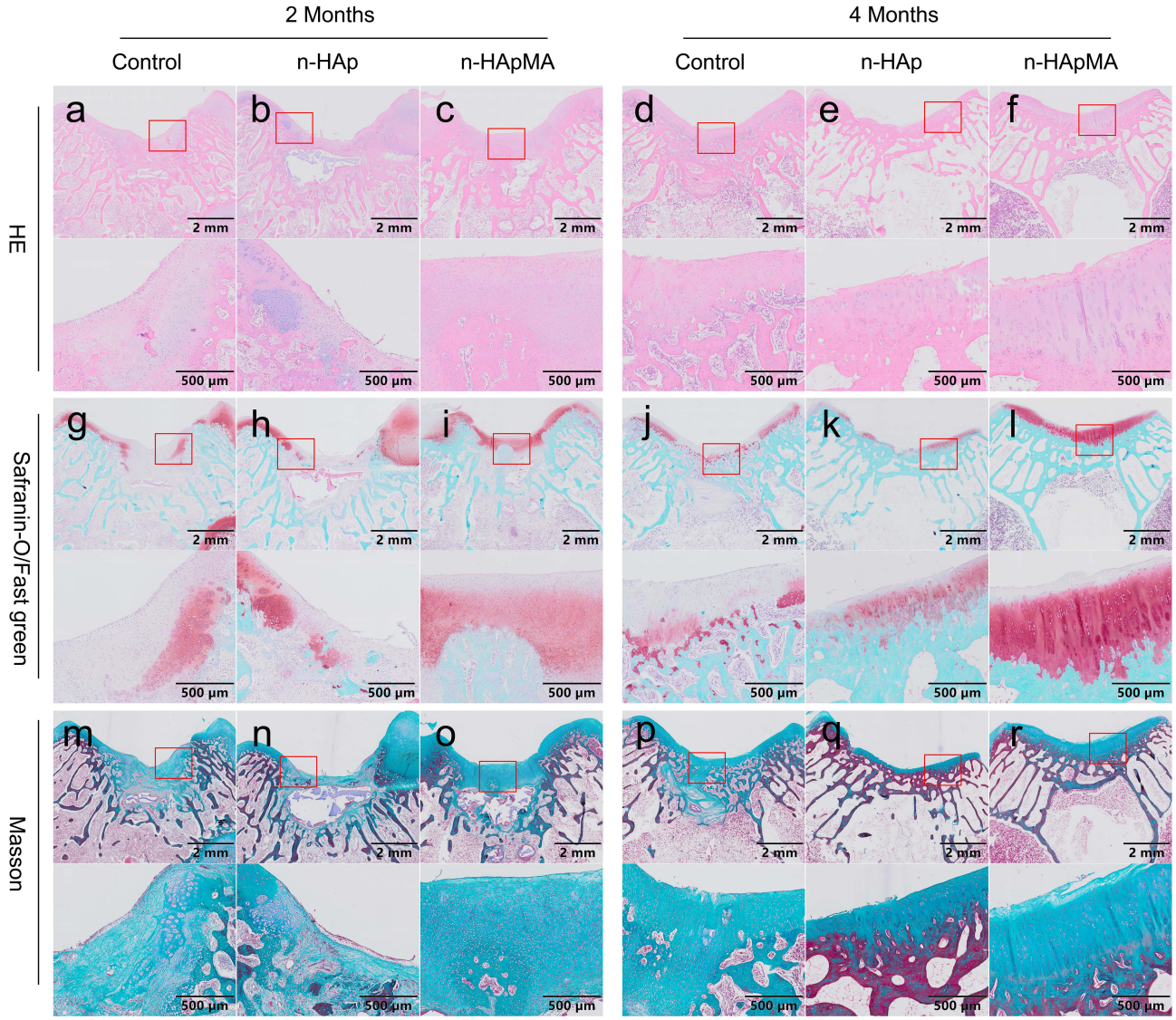


**Figure 5** (**a–f**) HE staining, (**g–l**) Safranin-O/Fast green staining and (**m–r**) Masson staining of femoral condyle samples in control, n-HAp and n-HApMA group.

area had cell density similar to the uninjured area, but the cartilage layer was thinner than in the uninjured area. The n-HApMA group's regenerated area had cell density similar to the uninjured area, an arrangement pattern similar to normal cartilage tissue but with more cells, and a thicker cartilage layer than the uninjured area (Figure 5d–f).

In Safranin O-Fast Green staining, normal cartilage tissue was stained red, and bone tissue was stained blue-green. At two months post-surgery, the control group's regenerated area boundary had some red-stained regions, but almost no blue-green staining area. The n-HAp group's regenerated area had a small amount of red staining and sporadic green staining areas, interwoven with red regions. The n-HApMA group's regenerated area surface was uniformly covered by red-stained regenerated cartilage, thicker than the uninjured area, and blue-green bone tissue appeared in the deep layer of the regenerated area, with cartilage thickness in regenerated bone tissue locations consistent with the uninjured area (Figure 5g–i). At four months post-surgery, the control group had a small amount of red cartilage tissue, but only in the deep layer, with a small amount of green bone tissue in the deeper layers of the cartilage. The n-HAp group's regenerated area had discontinuous red cartilage tissue, while the deeper bone tissue showed more repair. The n-HApMA group's regenerated area had thicker red cartilage than the uninjured area, with more bone tissue repair in the deeper layers and a structure more similar to normal bone tissue (Figure 5j–l).

In Masson staining, collagen fibers were stained blue. At two months post-surgery, most of the control group's regenerated area was blue, indicating the generation of a large amount of collagen fibers. Since Safranin O stains cartilage red and Masson staining stains collagen blue, it can be deduced that at two months post-surgery, only a small part of the control group's regenerated area was hyaline cartilage regeneration, while most were fibrocartilage composed of non-type II collagen. Similarly, at two months post-surgery, only a small part of the n-HAp group's regenerated area was hyaline cartilage, with most being fibrocartilage and scattered bone tissue regeneration. The n-HApMA group's regenerated area was mostly hyaline cartilage with some bone regeneration (Figure 5m–o). At four months post-surgery, the control group had almost completed fibrocartilage regeneration and had some bone tissue regeneration. The n-HAp group's regenerated cartilage layer had some hyaline cartilage and some fibrocartilage, with good bone tissue regeneration. The n-HApMA group achieved complete hyaline cartilage regeneration and also demonstrated good regeneration performance in the subchondral bone tissue (Figure 5p–r).

## Expression of Bone and Cartilage Markers

Six proteins were detected using immunohistochemical staining: Type I Collagen, Type II Collagen, Aggrecan, OCN, Sox9, and Runx2. Type I Collagen is the main collagen fiber type in bone tissue and fibrocartilage, while Type II Collagen exists only in hyaline cartilage. Aggrecan is a cartilage-specific proteoglycan highly expressed in cartilage tissue, while OCN is a bone-specific molecule secreted only by osteoblasts. Sox9 is one of the key transcription factors in chondrocyte differentiation, activating the transcription of Type II Collagen and Aggrecan, and plays an important role in cartilage development and maturation. Runx2 is one of the key transcription factors in osteoblast differentiation, promoting the osteogenic differentiation of mesenchymal stem cells and playing an essential role in bone formation.

Two months post-surgery, the regenerated area of the control group showed simultaneous expression of Type I and Type II Collagen, but only Aggrecan was highly expressed in the same area, and only a few cells were positive for OCN. Additionally, both Sox9 and Runx2 showed high expression in this area. These findings indicate that cartilage formation and bone formation were occurring simultaneously in the regenerated area of the control group, with active cartilage formation and early-stage bone formation (Figure 6a, g, m and s; Figure 7a and g).

Two months post-surgery, the regenerated area of the n-HAp group showed significant expression of Type I Collagen, with less expression of Type II Collagen. Aggrecan and OCN both displayed low expression, while Runx2 expression was higher and Sox9 expression was lower. These findings indicate that bone formation was the primary process in the regenerated area of the n-HAp group, occurring in the early stages, with less evident cartilage formation (Figure 6b, 6h, n and t; Figure 7b and h).

In contrast to the control and n-HAp groups, the surface layer of the regenerated area in the n-HApMA group showed low expression of Type I Collagen, Type II Collagen, Aggrecan, OCN, Sox9, and Runx2, indicating that the surface layer tissue had not yet undergone significant osteogenic or chondrogenic differentiation. In contrast, the deeper tissue layers showed high expression of Sox9, Runx2, Type I Collagen, Aggrecan, and OCN, with only low expression of Type II Collagen. These results

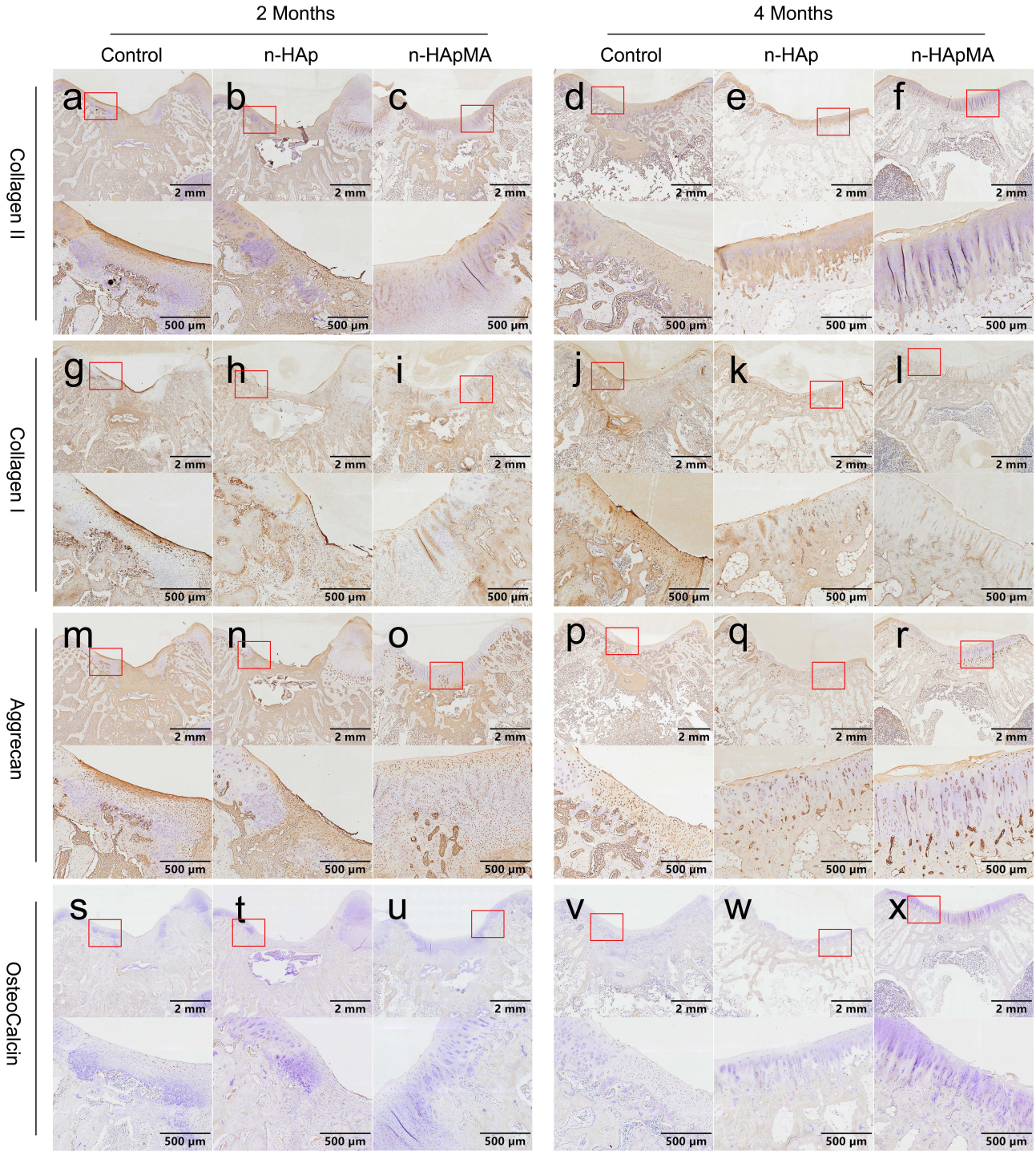


**Figure 6** Immunohistochemical staining of femoral condyle samples in control, nano-hydroxyapatite (n-HAp), and methacrylated nano-hydroxyapatite (n-HApMA) groups. (**a–f**) Collagen II, (**g–l**) Collagen I, (**m–r**) Aggrecan, (**s–x**) Osteocalcin.

suggest that bone and cartilage regeneration in the n-HApMA group began with chondrogenic differentiation in the deeper layers, gradually shifting towards osteogenic differentiation (Figure 6c, i, o and u; Figure 7c and i).

Four months post-surgery, the overall tissue regeneration of the control, n-HAp, and n-HApMA groups was better than at two months post-surgery. The regenerated area of the control group showed higher expression of Type I Collagen and lower expression of Type II Collagen at the surface layer. Aggrecan-positive cells still accounted for a high

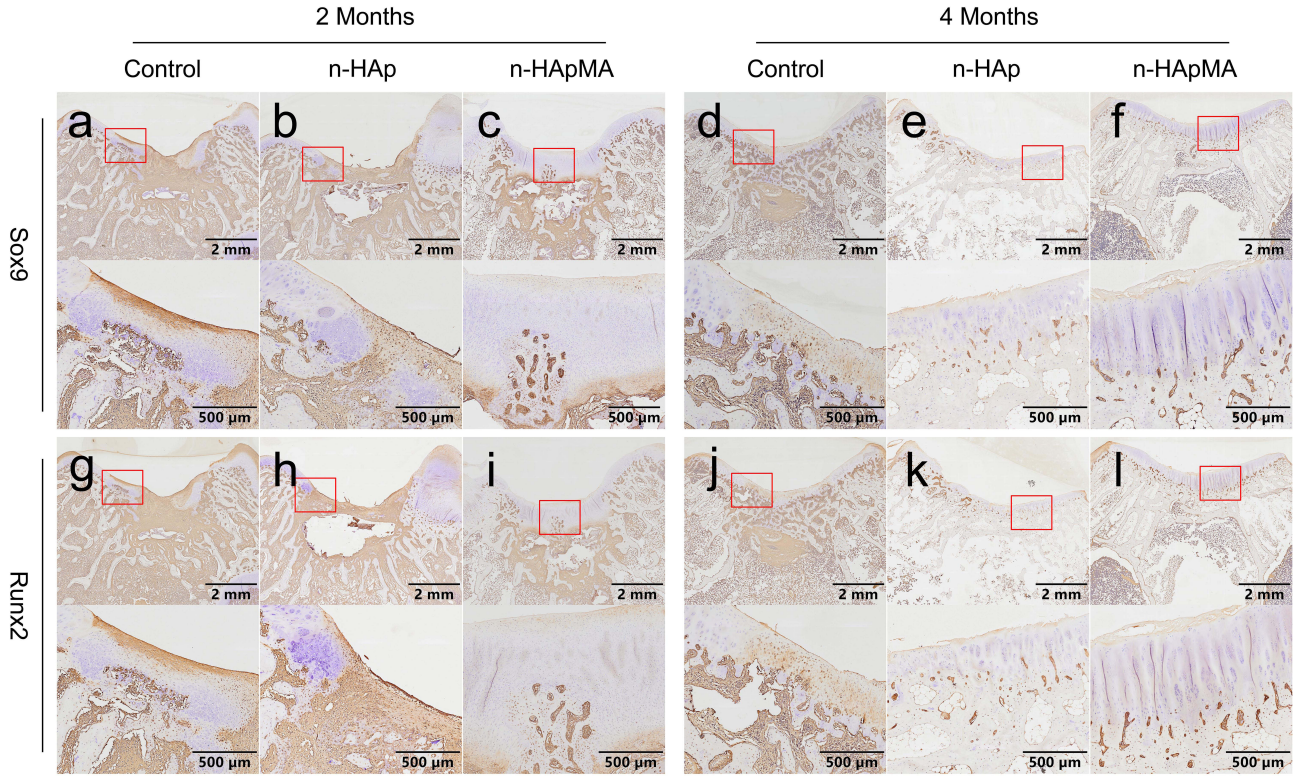


**Figure 7** Immunohistochemical staining of femoral condyle samples in control, nano-hydroxyapatite (n-HAp), and methacrylated nano-hydroxyapatite (n-HApMA) groups. (**a–f**) Sox9, (**g–l**) Runx2.

proportion, but there was a significant reduction in the extracellular matrix. The proportion of OCN-positive cells was significantly higher than at two months post-surgery. These results indicate that, four months post-surgery, the control group mainly formed fibrocartilage rather than hyaline cartilage in the regenerated area, with a certain tendency towards osteogenic differentiation (Figure 6d, j, p and v; Figure 7d and j).

Four months post-surgery, the regenerated area of the n-HAp group displayed a thinner cartilage layer than the control group, with higher expression of Type I Collagen and lower expression of Type II Collagen. Aggrecan-positive cells maintained a high proportion, while OCN-positive cells were lower in proportion. Sox9 and Runx2 positive cells were rarely observed in the regenerated cartilage layer, while they were more common in the subchondral bone area. These findings suggest that, four months post-surgery, the n-HAp group demonstrated stronger osteogenic differentiation compared to the control group, with less evident chondrogenic differentiation and a continued process of endochondral ossification in the subchondral bone area (Figure 6e, k and q, w; Figure 7e and k).

Four months post-surgery, the regenerated area of the n-HApMA group showed almost no expression of Type I Collagen in the surface layer, with abundant expression of Type II Collagen. At the same time, nearly all cells in the regenerated tissue surface layer displayed strong Aggrecan expression, while OCN was observed only in small amounts in the deeper cartilage layers. Sox9 and Runx2 showed no positive expression in the cartilage layer, with Runx2 only observed in some positive areas in the subchondral bone layer. These results indicate that, four months post-surgery, the n-HApMA group had largely completed the regeneration of cartilage and subchondral bone tissue, with only a small area still undergoing the differentiation process from cartilage to subchondral bone (Figure 6f, l, r and x; Figure 7f and l).

## Discussion

Osteoarthritis is a disease affecting the entire joint, involving not only the articular cartilage but also the subchondral bone and surrounding soft tissues. As a result, merely repairing the joint cartilage cannot achieve the therapeutic goals for osteoarthritis.[29,30] The subchondral bone not only provides physical support and blood supply to the cartilage but also

influences cartilage repair and osteoarthritis progression through cellular signaling pathways. Consequently, the integrated bone and cartilage repair has emerged as a new stage-specific objective in osteoarthritis treatment.[31,32] In this study, we attempted to approach the problem of osteochondral unit regeneration by improving the dispersion of nano-hydroxyapatite and constructing a biomimetic subchondral bone microenvironment, ultimately promoting better bone and cartilage regeneration.

We employed a hydrothermal synthesis method to chemically modify the surface of nano-hydroxyapatite (n-HAp).[22] The changes in average size and zeta potential suggest that the dispersion of hydroxyapatite has been enhanced after modification. The infrared spectra showed no noticeable C=O or C=C absorption peak after the modification, which could be attributed to the low amount of 3-(Trimethoxysilyl)propyl methacrylate (TMSPMA) used for modifying n-HAp. A comparison of the XRD patterns before and after modification revealed that the diffraction peak positions of the two samples did not change, indicating that the coupling agent modification did not alter the crystal structure or crystallinity of n-HAp. The differences in the TG and DSC curves of n-HAp and n-HApMA can be explained as follows. Both the raw n-HAp material and the modified n-HApMA contain free water, which evaporates first during the heating process. The modified groups on the surface of n-HApMA slow down the evaporation of free water. As the temperature increases to 300°C, the modified groups begin to decompose, and the water in n-HApMA, which has been slowed in evaporation, starts to evaporate in large quantities. When the temperature reaches 600°C, the free water has essentially evaporated completely, and the masses of n-HAp and n-HApMA become similar. Subsequently, the modified groups continue to decompose, and the bound water begins to be removed until the evaporation of the bound water is complete. Under conditions of 300–900°C, the modified groups remain in a decomposed state. The differences in the thermogravimetric analysis of the two samples can indirectly reflect the successful chemical modification of n-HApMA. In addition, an increase in mass by 0.8% after modification provides further indirect evidence of successful modification. Compared with several other studies, our modified hydroxyapatite did not show significant changes in FTIR.[33,34] The absence of discernible differences could be attributed to either inadequate surface modification or overlapping spectral features resulting from the presence of adsorbed water molecules.[35]

Although our nano-hydroxyapatite only had minor changes after modification, it showed significant differences when applied to bio-inks. Bio-inks are biocompatible materials, often composed of cells, biomolecules, and other supportive components, which can be utilized in 3D bioprinting for the fabrication of tissue constructs.[36] These inks facilitate the precise deposition of living cells and biological structures, enabling the creation of customized tissue models for research, drug testing, and regenerative medicine applications. Moreover, the versatility of bio-inks allows for tailoring their properties to meet specific requirements, thereby driving advancements in the field of tissue engineering.[37] In this study, a unique bio-ink formulation was developed by incorporating a specially designed porous modified gelatin, along with modified nano-hydroxyapatite particles, and adipose-derived stem cells. The combination of these components created a biocompatible material, enabling precise deposition of cellular structures and enhanced tissue engineering capabilities. When n-HApMA was mixed with high-porosity GelMA, we observed differences in the photocuring rheological test. The addition of 5% n-HApMA significantly increased the elastic modulus of 6% high-porosity GelMA to about three times its original value, whereas 5% n-HAp only resulted in approximately two times increase. This was further confirmed in compression tests, where the stiffness of bio-ink containing 5% n-HApMA and 6% high-porosity GelMA was about three times that of 6% high-porosity GelMA, whereas 5% n-HAp had only about two times effect. Both n-HAp and n-HApMA adhered to the walls formed by GelMA, as observed by SEM. The difference was that n-HApMA exhibited better adhesion uniformity than n-HAp. This “armor” of hydroxyapatite on GelMA can explain the increased elastic modulus of GelMA. Additionally, the uniform distribution pattern can ensure that mesenchymal stem cells adhere to the surface of hydroxyapatite rather than GelMA, thereby better promoting osteogenesis.

The live-dead staining results demonstrated that cells within the scaffolds of all three groups exhibited high survival rates and growth states. After implanting the scaffolds into rabbit osteochondral defect models, the n-HAp group showed better bone tissue regeneration compared to the control group. Although the n-HAp group also displayed some cartilage regeneration, the effect was not superior to the control group, and the regenerated cartilage was mainly fibrocartilage rather than hyaline cartilage. However, the n-HApMA group exhibited better bone repair in terms of both speed and proportion compared to the control and n-HAp groups, with satisfactory hyaline cartilage regeneration. Although the regenerated cartilage in the

superficial layer of the n-HApMA group did not exhibit a dense horizontal cell arrangement as seen in the physiological state, cells displayed a similar bundle-like arrangement in the vertical direction. Images of the n-HApMA group also revealed the presence of "chondrocyte lacunae" and pairs of neighboring cells formed due to proliferation. Additionally, the thickness and quality of the cartilage in the n-HApMA group were not inferior to those in the non-modeled area.

The study results indicated that the addition of n-HAp or n-HApMA could accelerate bone regeneration, but the speed of cartilage regeneration was not significantly affected. In terms of cartilage regeneration quality, the n-HAp group was similar to the control group, mainly characterized by fibrocartilage regeneration, while the n-HApMA group primarily exhibited hyaline cartilage regeneration. Comparing the various staining results at 2 and 4 months post-surgery, bone regeneration in the control, n-HAp, and n-HApMA groups all began with cartilage regeneration, followed by bone regeneration through endochondral ossification.

In this study, no drugs or growth factors promoting cartilage regeneration were added. The biphasic scaffolds only had n-HAp or n-HApMA incorporated into the subchondral bone layer for bone regeneration promotion. However, the results showed that the addition of n-HApMA not only accelerated the speed of bone regeneration but also improved the quality of cartilage regeneration.

## Conclusion

In summary, this study investigated the effects of surface-modified nano-hydroxyapatite (n-HApMA) in enhancing osteochondral regeneration when combined with high-porosity GelMA. The n-HApMA was successfully synthesized and characterized, demonstrating improved dispersion compared to unmodified n-HAp. The incorporation of n-HApMA into GelMA significantly increased the elastic modulus of the resulting bio-ink, leading to improved mechanical properties. When implanted into a rabbit osteochondral defect model, scaffolds containing n-HApMA exhibited superior osteochondral regeneration compared to the control group and n-HAp group. The regenerated cartilage in the n-HApMA group showed a similar vertical cell arrangement to physiological conditions, along with chondrocyte lacunae and pairs of neighboring cells. These findings suggest that the addition of n-HApMA to high-porosity GelMA scaffolds not only accelerates bone regeneration but also enhances cartilage regeneration quality, making it a promising material for osteochondral tissue engineering applications.

## Acknowledgments

This work was financially supported by the National Natural Science Foundation of China (81972042, 82072400), the Natural Science Foundation of Jiangsu Province (BK20200001, BE2019736, and BE2019679), and Jiangsu Province Traditional Chinese Medicine Science and Technology Development Plan for Young Talents Project (QN202113).

## Disclosure

The authors report no conflicts of interest in this work.

## References

1. Hunter DJ, Bierma-Zeinstra S. Osteoarthritis. *Lancet*. 2019;393(10182):1745–1759. doi:10.1016/S0140-6736(19)30417-9
2. Chen T, Weng W, Liu Y, et al. Update on novel non-operative treatment for osteoarthritis: current status and future trends. *Front Pharmacol*. 2021;12:755230. doi:10.3389/fphar.2021.755230
3. Akhavan S, Martinkovich SC, Kasik C, et al. Bone marrow edema, clinical significance, and treatment options: a review. *J Am Acad Orthop Surg*. 2020;28(20):e888–e899. doi:10.5435/JAAOS-D-20-00142
4. Liu Y, Shah KM, Luo J. Strategies for articular cartilage repair and regeneration. *Front Bioeng Biotechnol*. 2021;9:770655. doi:10.3389/fbioe.2021.770655
5. Vinatier C, Guicheux J. Cartilage tissue engineering: from biomaterials and stem cells to osteoarthritis treatments. *Ann Phys Rehabil Med*. 2016;59(3):139–144. doi:10.1016/j.rehab.2016.03.002
6. O'Brien FJ. Biomaterials & scaffolds for tissue engineering. *Materials Today*. 2011;14(3):88–95. doi:10.1016/S1369-7021(11)70058-X
7. Pittenger MF, Discher DE, Péault BM, et al. Mesenchymal stem cell perspective: cell biology to clinical progress. *NPJ Regen Med*. 2019;4(1):22. doi:10.1038/s41536-019-0083-6
8. Cao Y, Jansen IDC, Sprangers S, et al. IL-1beta differently stimulates proliferation and multinucleation of distinct mouse bone marrow osteoclast precursor subsets. *J Leukoc Biol*. 2016;100(3):513–523. doi:10.1189/jlb.1A1215-543R
9. Dai J, Dong R, Han X, et al. Osteoclast-derived exosomal let-7a-5p targets Smad2 to promote the hypertrophic differentiation of chondrocytes. *Am J Physiol Cell Physiol*. 2020;319:C21–C33. doi:10.1152/ajpcell.00039.2020

10. Fujisawa T, Hattori T, Takahashi K, et al. Cyclic mechanical stress induces extracellular matrix degradation in cultured chondrocytes via gene expression of matrix metalloproteinases and interleukin-1. *J Biochem*. 1999;125(5):966–975. doi:10.1093/oxfordjournals.jbchem.a022376
11. Jung YK, Han M-S, Park H-R, et al. Calcium-phosphate complex increased during subchondral bone remodeling affects earlystage osteoarthritis. *Sci Rep*. 2018;8(1):487. doi:10.1038/s41598-017-18946-y
12. Peng Y, Wu S, Li Y, et al. Type H blood vessels in bone modeling and remodeling. *Theranostics*. 2020;10(1):426–436. doi:10.7150/thno.34126
13. Romeo SG, Alawi KM, Rodrigues J, et al. Endothelial proteolytic activity and interaction with non-resorbing osteoclasts mediate bone elongation. *Nat Cell Biol*. 2019;21(4):430–441. doi:10.1038/s41556-019-0304-7
14. Zhen G, Cao X. Targeting TGFbeta signaling in subchondral bone and articular cartilage homeostasis. *Trends Pharmacol Sci*. 2014;35(5):227–236. doi:10.1016/j.tips.2014.03.005
15. Hu Y, Chen X, Wang S, et al. Subchondral bone microenvironment in osteoarthritis and pain. *Bone Res*. 2021;9(1):20. doi:10.1038/s41413-021-00147-z
16. Kavasi RM, Coelho CC, Platania V, et al. In vitro biocompatibility assessment of nano-hydroxyapatite. *Nanomaterials*. 2021;11(5):1152. doi:10.3390/nano11051152
17. Chang BS, Lee CK, Hong K-S, et al. Osteoconduction at porous hydroxyapatite with various pore configurations. *Biomaterials*. 2000;21 (12):1291–1298. doi:10.1016/S0142-9612(00)00030-2
18. Bal Z, Kaito T, Korkusuz F, et al. Bone regeneration with hydroxyapatite-based biomaterials. *Emerg Mat*. 2019;3(4):521–544. doi:10.1007/s42247-019-00063-3
19. Wang K, Cheng W, Ding Z, et al. Injectable silk/hydroxyapatite nanocomposite hydrogels with vascularization capacity for bone regeneration. *J Mater Sci Technol*. 2021;63:172–181. doi:10.1016/j.jmst.2020.02.030
20. Zhou H, Lee J. Nanoscale hydroxyapatite particles for bone tissue engineering. *Acta Biomater*. 2011;7(7):2769–2781. doi:10.1016/j.actbio.2011.03.019
21. Tien Lam N, Minh Quan V, Boonrungsiman S, et al. Effectiveness of bio-dispersant in homogenizing hydroxyapatite for proliferation and differentiation of osteoblast. *J Colloid Interface Sci*. 2022;611:491–502. doi:10.1016/j.jcis.2021.12.088
22. Nabipour H, Batool S, Hu Y. Chemical surface modification of hydroxyapatite for biomedical application: a review. *Emerg Mat*. 2021;6(1):31–44. doi:10.1007/s42247-021-00322-2
23. Shuai C, Yu L, Feng P, et al. Interfacial reinforcement in bioceramic/biopolymer composite bone scaffold: the role of coupling agent. *Colloids Surf B Biointerfaces*. 2020;193:111083. doi:10.1016/j.colsurfb.2020.111083
24. Bareiro O, Santos LA. Tetraethylorthosilicate (TEOS) applied in the surface modification of hydroxyapatite to develop polydimethylsiloxane/hydroxyapatite composites. *Colloids Surf B Biointerfaces*. 2014;115:400–405. doi:10.1016/j.colsurfb.2013.12.027
25. Abbasi N, Hamlet S, Love RM, et al. Porous scaffolds for bone regeneration. *J Sci*. 2020;5(1):1–9.
26. Mohammadi H, Sepantafar M, Muhamad N, et al. How does scaffold porosity conduct bone tissue regeneration? *Adv Eng Mater*. 2021;23(10). doi:10.1002/adem.202100463
27. Saiz E, Gremillard L, Menendez G, et al. Preparation of porous hydroxyapatite scaffolds. *Mater Sci Eng*. 2007;27(3):546–550. doi:10.1016/j.msec.2006.05.038
28. Sánchez-Salcedo S, Arcos D, Vallet-Regí M. Upgrading calcium phosphate scaffolds for tissue engineering applications. *Key Eng Mater*. 2008;377:19–42. doi:10.4028/www.scientific.net/KEM.377.19
29. Hu W, Chen Y, Dou C, et al. Microenvironment in subchondral bone: predominant regulator for the treatment of osteoarthritis. *Ann Rheum Dis*. 2021;80(4):413–422. doi:10.1136/annrheumdis-2020-218089
30. Chen D, Shen J, Zhao W, et al. Osteoarthritis: toward a comprehensive understanding of pathological mechanism. *Bone Res*. 2017;5:16044. doi:10.1038/boneres.2016.44
31. Zhen G, Wen C, Jia X, et al. Inhibition of TGF-beta signaling in mesenchymal stem cells of subchondral bone attenuates osteoarthritis. *Nat Med*. 2013;19(6):704–712. doi:10.1038/nm.3143
32. Imhof H, Breitenseher M, Kainberger F, et al. Importance of subchondral bone to articular cartilage in health and disease. *Top Magn Reson Imaging*. 1999;10(3):180–192. doi:10.1097/00002142-199906000-00002
33. Mohandes F, Salavati-Niasari M. Particle size and shape modification of hydroxyapatite nanostructures synthesized via a complexing agent-assisted route. *Mater Sci Eng C Mater Biol Appl*. 2014;40:288–298. doi:10.1016/j.msec.2014.04.008
34. Zhang J, Lu P, Teng Y, et al. In-situ surface modification of precipitated silica nanoparticles with 3-methacryloxypropyltrimethoxysilane in carbonation process. *Res Chem Intermed*. 2021;47(7):3037–3050. doi:10.1007/s11164-021-04452-4
35. Huysal M, Senel M. Dendrimer functional hydroxyapatite nanoparticles generated by functionalization with siloxane-cored PAMAM dendrons. *J Colloid Interface Sci*. 2017;500:105–112. doi:10.1016/j.jcis.2017.04.004
36. Lim KS, Galarraga JH, Cui X, et al. Fundamentals and applications of photo-cross-linking in bioprinting. *Chem Rev*. 2020;120(19):10662–10694. doi:10.1021/acs.chemrev.9b00812
37. Kim BS, Das S, Jang J, et al. Decellularized extracellular matrix-based bioinks for engineering tissue- and organ-specific microenvironments. *Chem Rev*. 2020;120(19):10608–10661. doi:10.1021/acs.chemrev.9b00808